

H β line shape and radius-luminosity relation in 2.5D FRADO

M. H. Naddaf^{1,*}, M. L. Martinez-Aldama^{2,3,4}, D. Hutsemékers¹, D. Savic¹, and B. Czerny⁵

¹ Institut d'Astrophysique et de Géophysique, Université de Liège, Allée du six août 19c, B-4000 Liège (Sart-Tilman), Belgium

² Astronomy Department, Universidad de Concepción, Barrio Universitario S/N, Concepción 4030000, Chile

³ Millennium Nucleus on Transversal Research and Technology to Explore Supermassive Black Holes (TITANs), Concepción, Chile

⁴ Millennium Institute of Astrophysics (MAS), Nuncio Monseñor Sotero Sanz 100, Providencia, Santiago, Chile

⁵ Center for Theoretical Physics, Polish Academy of Sciences, Al. Lotników 32/46, 02-668 Warsaw, Poland

Submitted: May 2025

ABSTRACT

Context. Galaxies with active galactic nuclei (AGN) exhibit broad emission lines as a key spectral feature. The shape of emission-line profiles depends on the complex dynamics of discrete clouds within a spatially extended region known as the Broad Line Region (BLR). The distribution of cloud positions within BLR, or the geometry of BLR indeed, is directly linked to measurements of time lags of BLR.

Aims. In this paper, we convolve a large grid of physically-based simulations of cloud distributions in BLR with photon-flux weighted emissivity of BLR clouds to investigate the generic shape of spectral line profiles. More importantly, we extract the time-delay histograms of corresponding models to calculate the size of BLR.

Methods. Our physical model is based on the assumption that the clouds are launched by the radiation pressure acting on dust in the atmosphere of the outer disk. It has very few global parameters. The model is appropriate for the low ionization part of the BLR, as it was shown by earlier model tests. It uses a non-hydrodynamical single-cloud approach to the BLR dynamics. In this way we simulate the distribution of positions and velocities of the clouds.

Results. We found that the width of line profiles gets broader with black hole mass, or with viewing angle, and gets narrower with accretion rate. The blue wing of the emission line profiles becomes more pronounced with increasing black hole mass and accretion rate, consistent with the formation and intensification of an outflow structure. We also found that the peak time-delays rather than averaged delay values better represents the observational trend and also the scatter in the radius-luminosity relation.

Key words. Active Galaxies – Broad Line Region – Main Sequence of Quasars – time-delays – Eigenvector 1 – Broad Emission Lines

1. Introduction

Broad emission lines in the optical-UV spectra of active galactic nuclei (AGNs) are distinct features characterized by their significant width of several 1000 km/s. These lines are generated in the broad line region (BLR), a spatially extended region close to the supermassive black hole at the center of an AGN (Seyfert 1943; Schmidt 1963). The BLR consists of dense, rapidly moving clouds of gas that are photoionized by the intense optical-UV continuum radiation emitted from the accretion disk surrounding the black hole. As a result, these clouds emit spectral lines that are Doppler-broadened due to their high velocities, and sometimes even relativistically-broadened if close enough to the central black hole, leading to the observed broad emission line profiles in the spectra of AGNs (Baldwin 1997; Krolik 1999; Sulentic et al. 2000; Bianchi et al. 2019).

Studies imply that BLR is universally present for accreting supermassive black holes, either in type I AGNs where the BLR is not obscured by the torus (Antonucci 1993), or in type II AGNs where the scattered polarized light can reveal the broad lines (Antonucci & Miller 1985); unless the luminosity, or correspondingly the accretion rate, is very low (Sabra et al. 2003; Genzel et al. 2010; Eckart et al. 2017). This indicates that the presence of BLR depends on the accretion rate (Czerny et al. 2004; Elitzur & Ho 2009; Du et al. 2015a, 2018; Naddaf et al.

2021; Naddaf & Czerny 2022). Although some sources with low accretion rates are claimed to have BLR (Bianchi et al. 2019), in most low luminosity sources a hot optically thin flow replaces the inner standard disk, the BLR becomes reduced to a relatively narrow ring (see e.g. Eracleous et al. 2009, for a review), and the emission seems to come directly from the illuminated disk surface. The details of the disappearance of the cold disk by the BLR are not well understood yet (e.g. Liu et al. 1999; Rózańska & Czerny 2000; Nicastro et al. 2003; Czerny et al. 2004; Liu & Qiao 2022) and may depend on the presence of the magnetic field and hot plasma surrounding the nucleus. In the extreme cases like Sgr A* neither cold disk nor BLR are present.

BLR are generally spatially unresolved apart from the recent interferometric measurements for 7 sources (Gravity Collaboration et al. 2018, 2021, 2020; GRAVITY Collaboration et al. 2024). However, the variability of the central source and the delayed response of BLR to variations in the continuum allows for the measurement of the characteristic distance from BLR to the central black hole. Given the constancy of the speed of light, c , the distance is $R_{\text{BLR}} = c\tau$, where τ represents the time lag between the continuum and a selected BLR emission line, which is measured using the reverberation mapping (RM) technique (Blandford & McKee 1982; Peterson 1993, 2014). The technique involves monitoring the AGN continuum (typically measured at 5100 Å) and broad emission lines (most notably, H β) over the extended periods. Combining the BLR radius with

* mh.naddaf@uliege.be

the broad emission-line velocity width yields the virial mass enclosed within the BLR, which is dominated by the black hole (Peterson et al. 1998; Kaspi et al. 2000). The validity of reverberation masses is supported by other means, for example by the consistency of reverberation-measured masses with other dynamical mass measurement methods (Davies et al. 2006; Onken et al. 2007; Hicks & Malkan 2008).

Optical reverberation mapping studies using the $H\beta$ line have shown a simple power-law relation of the form $R_{\text{BLR}} = L_{\lambda}^{\alpha}$ between the size of the BLR and the monochromatic luminosity of AGNs at 5100 Å (Kaspi et al. 2000; Peterson et al. 2004), known as radius-luminosity (R-L) relation. The α is typically close to 0.5 for $H\beta$ emission lines. But despite the success of R-L relation, it exhibits a scatter, which has increased with the accumulation of more sources (Du et al. 2015b). The scatter has been attributed to accretion-rate dependence of the BLR structure, with highly accreting sources showing the largest departures from the nominal R-L relation (Du et al. 2015b, 2018). Corrections based on the Eddington ratio and dimensionless accretion rate have been proposed to reduce this scatter (Martínez-Aldama et al. 2019). Other efforts to reduce this scatter include adjustments based on the Eddington ratio and dimensionless accretion rate, with significant progress achieved by incorporating the relative Fe II strength, which correlates with accretion-rate intensity (Du & Wang 2019).

Despite significant efforts by many researchers to reduce the scatter in the R-L relation, the topic remains an open question, with ongoing investigations from both theoretical and observational perspectives. The scatter is not confined to the R-L relation derived from reverberation-measured $H\beta$ time-delays, but also extends to other emission lines such as Mg II and C IV. This ongoing challenge motivates further exploration of the underlying causes of the scatter in different emission lines.

One more interesting topic is the use of BLR time delay for cosmology. The idea was outlined recently (Watson et al. 2011; Czerny et al. 2013; Martínez-Aldama et al. 2019), and some applications were made (Khadka et al. 2021; Cao et al. 2022, 2024) but they were based on parametric approach to the radius-luminosity relation. Without external calibration this approach can bring the results from the curvature of the Hubble diagram, constraining the Ω_m but not the Hubble constant. However, with physically motivated model predicting the position of the BLR for a given source intrinsic (absolute) luminosity it would be also possible to measure the Hubble constant by combining the time delay observations with the observed source flux.

In this paper, we approach the problem of the BLR properties from the theoretical side, without referring yet directly to observational data for specific objects. We present simulation results of geometry and dynamics of BLR using our 2.5D FRADO (Failed Radiatively Accelerated Dusty Outflow) model, which specifically accounts for the lowly-ionized part of the BLR (Naddaf et al. 2021). From our simulations, we calculate the theoretical transfer function, mapping BLR, determine a representative single-value delay and compare the results representing a distribution of the global parameters with the observational trends in the R-L relation. Therefore we structure the paper as follows. In section 2, we present the modeling of the BLR. Section 3 details the computation of emission line profiles based on our model, followed by section 4 where we address the calculation of time-delay maps and extraction of R-L relation from our simulations. In section 6 we discuss the results, and finally, we conclude the paper in section 7.

2. Modeling the BLR

In order to model the BLR we use 2.5D FRADO model, based on a physically motivated mechanism of dust-driven outflow from the disk surface in the region where the disk surface temperature is lower than the sublimation temperature. This assumption localizes the position of the BLR and cloud dynamics, thus the model, unlike the parametric models of BLR (e.g. Pancoast et al. 2011, 2012; Li et al. 2013), is not based on arbitrary parametrization of the cloud position. The model uses a non-hydro single-cloud approach to the dynamics of BLR.

2.1. The 2.5D FRADO

The FRADO model describes the formation of the BLR in an AGN. This model is based on the concept that radiation pressure acts on dust in the regions of the accretion disk where the temperature of the disk atmosphere is below the dust sublimation threshold. According to FRADO, this mechanism is responsible for the uplift of material that contributes to the emission of low-ionization lines. The model was initially proposed by Czerny & Hryniewicz (2011) and further enhanced to 2.5 dimension in (Naddaf et al. 2021). The model posits that radiative pressure on dust lifts clouds from the disk surface, preserving their angular momentum derived from the Keplerian motion of the disk. Once lifted, these clouds are more strongly illuminated by the inner disk regions. If a cloud becomes too hot, the dust evaporates, and the cloud continues its motion along a ballistic orbit. The global parameters of the model are the black hole mass, the Eddington rate, and the metallicity. Under conditions of lower black hole mass, lower Eddington ratio, and lower metallicity, the clouds form only a failed wind. Conversely, in scenarios of higher black hole mass, higher Eddington ratio, and higher metallicity, a fraction of the clouds may form an escaping wind. Early tests of the model (Czerny et al. 2015; Naddaf & Czerny 2022, 2024) looked promising, in particular the application of the model to the broad absorption line quasars was attractive (Naddaf et al. 2023). Now we aim to test the model more systematically.

By knowing the global parameters of the source, we can determine the 3-D locations of statistically representative clouds and their velocities. The computational method of the dynamics of the single cloud is described in detail by Naddaf et al. (2021). We then combine the cloud positions and velocities with this the emissivity law for a specific emission line, applying the model to low-ionization lines such as $H\beta$, Mg II, or Fe II.

2.2. simulation setup and the grid of models

In order to perform a comprehensive study, we assumed a wide-range of black hole masses ($\log M_{\bullet}$ from 6 to 10 in solar units), and accretion rates ($\log \dot{m}$ from -2 to 0 in Eddington units), both binned with 0.2 dex. Such a grid of models corresponds well to the parameter range seen in quasar catalog (Shen et al. 2011). Sublimation temperature of dust is kept at 1500 K (Barvainis 1987), and metallicity is set at 5 times solar, equivalent to dust-to-gas mass ratio of 0.025 (Baskin & Laor 2018; Naddaf & Czerny 2022). The adopted range of the viewing angles cover the range from 10° to 60° , with the step of 5° . Larger viewing angles are not considered since for such sources the BLR is generally shielded by the dusty torus, and objects are classified as type 2, with only narrow lines visible in the unpolarized spectra (see Krolik 1999, for a general review).

3. LIL BLR line profiles

3.1. Method of line profile modeling

Given a distribution of BLR clouds along with their velocity field and local emissivity, one can find the shape of emission line profiles. As the LIL BLR locates at the radii larger than at least a few $100 r_g$ (regardless of the black hole mass), the gravitational redshift may safely be neglected and only the Doppler effect contributes to line broadening. Previously, we assumed that the BLR simply follows a single-emissivity function weighted with the vertical position of a given cloud in the ensemble of clouds forming the BLR (Naddaf & Czerny 2022). Now, in a more sophisticated manner, the line emissivity is computed convolving with the location-dependent flux of ionizing photons, $\phi_H(r)$.

Cloud are also assumed to be optically-thin so that each cloud is spherically uniformly illuminated (i.e. no "moon effect") and it then transforms the absorbed radiation into isotropic line emission. Preliminary BLR simulation studies were done for 2.5D FRADO model by Naddaf et al. (2021); Naddaf & Czerny (2022). Here we do a systematic survey, aimed additionally at modeling the time delay. We use a universal ratio for the conversion of the local irradiating flux to line luminosity for all clouds. We assume that the line emissivity for $H\beta$ line roughly scales with the logarithm of the photon-flux which is a function of the cloud's location (Gilbert & Peterson 2003; Korista & Goad 2004). In photoionization equilibrium, the flux of hydrogen recombination lines such as $H\beta$ generally scales with the number of ionization per unit volume, which itself is tied to the incident ionizing photon flux ϕ . At low ϕ , this relation is approximately linear; however, at higher photon fluxes, due to saturation effects in ionization and optical depth, the scaling becomes sub-linear (more slowly than linearly). This is consistent with expectations for ionization-bounded or partially matter-bounded regimes where increased ionizing photon flux leads to diminishing increases in line emission due to saturation and thermal balance constraints. Simulations performed with the code CLOUDY (Ferland et al. 1996; Moloney & Shull 2014; Kriss et al. 2019; Temple et al. 2021; Chatzikos et al. 2023; Pandey et al. 2023) justify our approach revealing that a logarithmic scaling of $H\beta$ emissivity with ϕ provides an excellent empirical fit. The figure 1 shows the $H\beta$ line emissivity (flux) as a function of the photon flux ϕ , for $\phi > \sim 10^{17}$ photons $\text{cm}^{-2} \text{s}^{-1}$ (Ashwani Pandey; private communications). The photon flux and the ionizing continuum spectral energy distribution (SED) with respect to the location of each cloud are directly computed from the 2.5 FRADO. These are then input into CLOUDY along with gas density, n_H of 10^{11} cm^{-3} , and column density, N_H of 10^{23} cm^{-2} . As can be seen, in the first approximation it implies a non-linear behavior of $H\beta$ with respect to photon flux, well approximated as a logarithmic trend (also see figure 2 in Gilbert & Peterson 2003, for NGC 5548 as an analogy).

3.2. Results

3.2.1. Dependence of line shapes on global parameters

Figures 2, 3, and 4, show the results for the LIL emission line profiles from the entire grid defined in section 2.2. Since the adopted scaling with the incident flux was tested for $H\beta$ line, the results below predominantly apply to this line.

The figure 2 shows the line profiles at representative observer's viewing angle of 39° (Lawrence & Elvis 2010) for varying black hole masses and for different Eddington ratios as indicated in the legend. For small black hole masses only high values

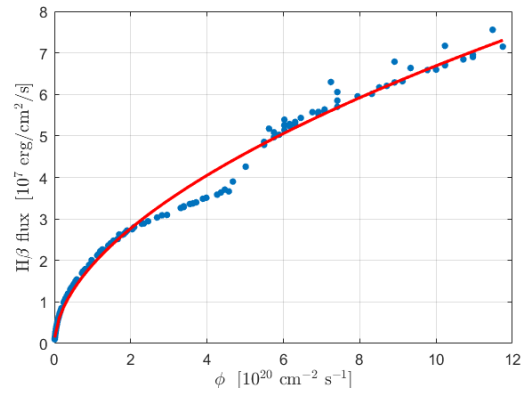


Fig. 1. Results from a CLOUDY simulation (Ashwani Pandey; private communications) for a range of photon flux (calculated by 2.5 FRADO) reaching a cloud in BLR. The plot depicting the $H\beta$ line emissivity (flux) as a function of the photon flux ϕ , implies an obviously non-linear (logarithmic) relation between these two. The blue points represent the simulation results, and the red curve shows a fit.

of the Eddington ratios are shown since at too low value of the Eddington ratio even the failed wind is not launched. In this case the lines can form in the disk itself but the inner radius is then not necessarily specified by the FRADO model. We address this issue in the Discussion. As the black hole mass increases, the profiles become broader. This is expected as the gravitational potential well deepens, leading to higher orbital velocities for material forming the BLR, thus reflected in the increasing width of the profiles. Particularly for lower masses the line profiles show a pronounced double-peaked structure. This is indicative of a disk-like dominated geometry of BLR (e.g. Eracleous & Halpern 1994). This happens for all Eddington rates, when FRADO solution exits. This is not consistent with observational data, as for high Eddington rates and small masses the observed line profiles are single-peaked (e.g. Moran et al. 1996; Laor et al. 1997; Véron-Cetty et al. 2001; Cracco et al. 2016). This suggests that the vertical velocity is underestimated in FRADO for small black hole mass. The feature diminishes for higher masses, where the line profiles are more dominated by a single broad component for high accretion rates, while the double peak is still observed in the low accretion regime. This is consistent with observational trends.

The figure 3 explores the dependence of the $H\beta$ line profile on Eddington ratio while keeping the black hole mass constant in each panel, for a range of masses between 6 to 10, and for the mean viewing angle 39° . As the accretion rate increases, the $H\beta$ line profiles generally become narrower, with the Full Width at Half Maximum (FWHM) changing from $\sim 10^4$ km/s down to $\sim 10^3$ km/s. However, with the rising accretion rate line asymmetry develops, with blueshifted tail. At the very high accretion rates, close to the Eddington rate, and high masses the line becomes broad again since most of the emission is emitted in an outflow. Lower accretion rates are typically associated with lower radiation pressure and weaker (or nonexistent) outflows, BLR forms closer to the black hole, which means that the gas in the broad-line region (BLR) can be more gravitationally bound and move with higher orbital velocities, leading to broader and double-peaked line profiles. Conversely, at higher accretion rates, the radiation pressure and outflows can dominate, driving winds and possibly increasing turbulence in the BLR. This can introduce more complex velocity structures, and blue asymmetric profiles as radiation pressure pushes gas away, particularly close to the Eddington ratio. This aligns with obser-

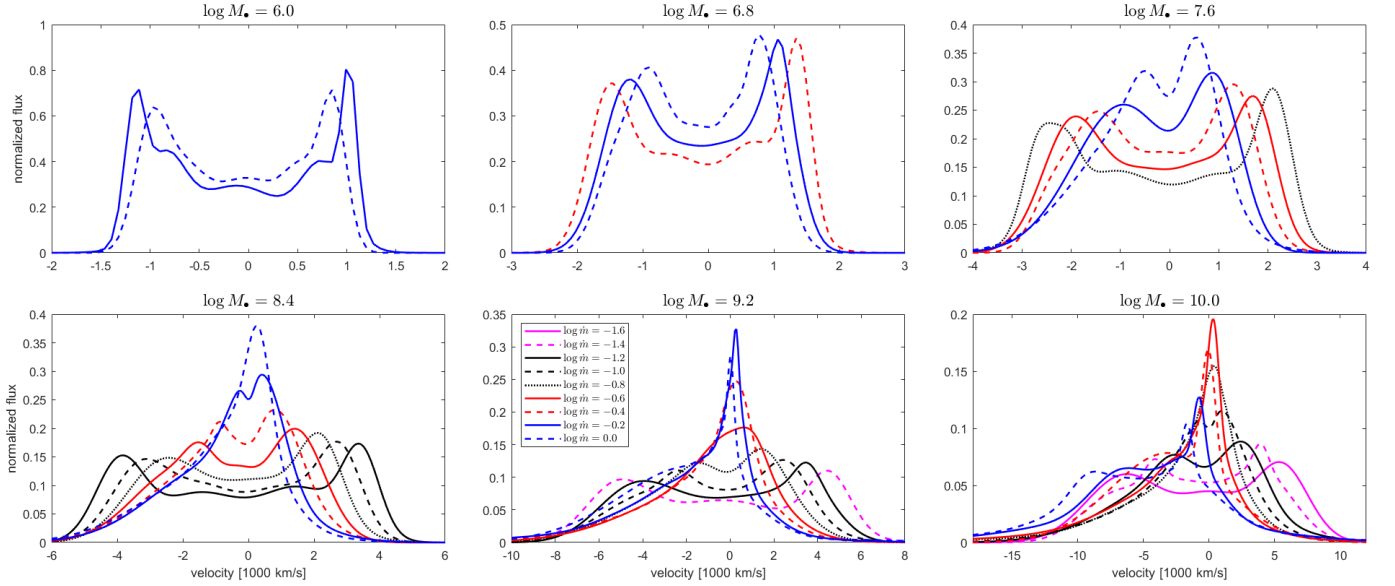


Fig. 2. Predicted shape of $H\beta$ line profiles divided into subgroups with respect to the black hole mass, and a viewing angle of 39° . Different lines in each panel mark representative Eddington ratio (see text). Note that the horizontal axis in each panel is different. The total flux of each line is normalized to one.

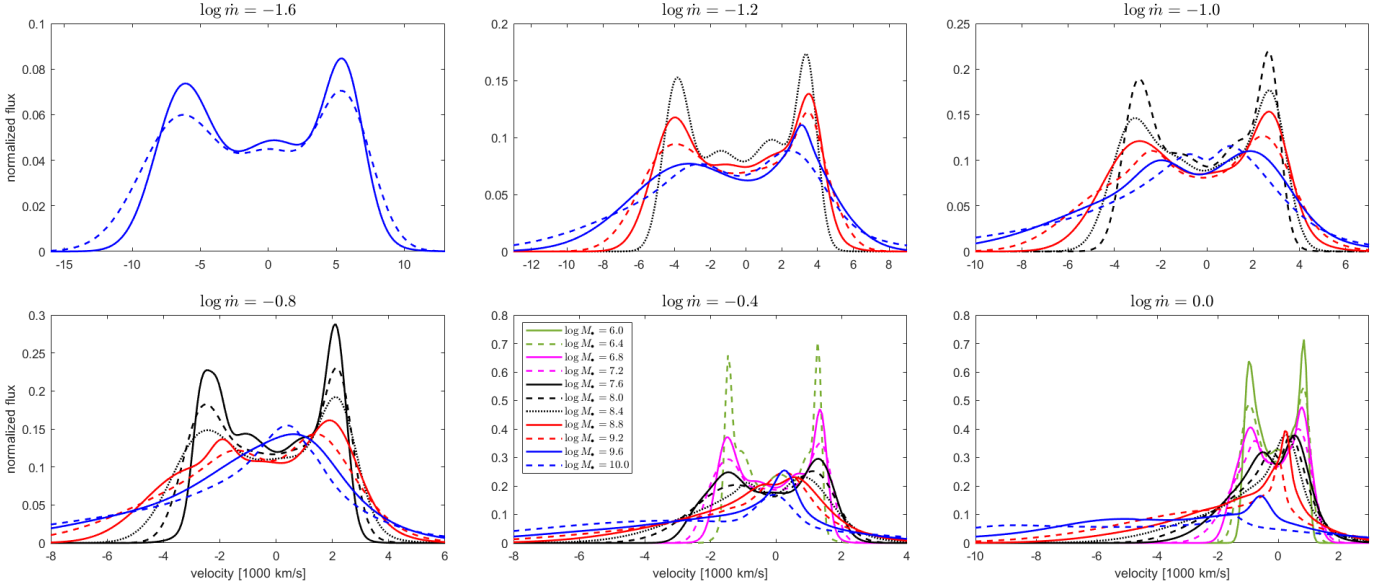


Fig. 3. Predicted shape of $H\beta$ line profiles divided into subgroups with respect to the Eddington ratio, and a viewing angle of 39° . Different lines in each panel mark representative black hole mass (see text). Note that the horizontal axis in each panel is different. The total flux of each line profile is normalized to one.

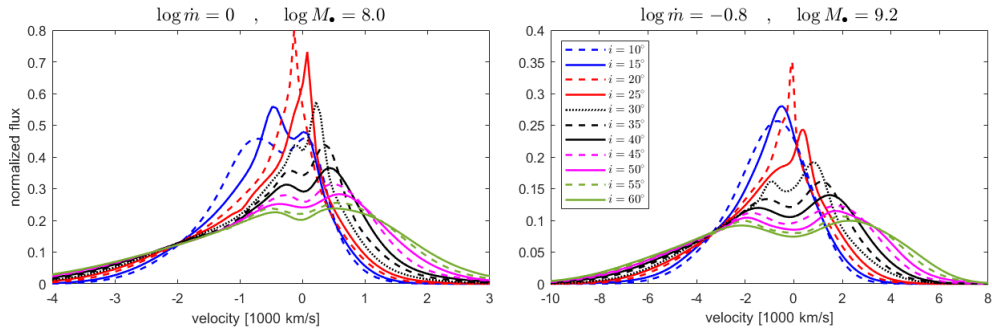


Fig. 4. Dependence of the line shape on viewing angle. The results are displayed for two specific models in our grid. Left panel stand for the canonic model of AGN and the right panel represents the model corresponding to the mean quasar. The total flux of each line is normalized to one.

vational studies where AGNs with high accretion rates (near or above the Eddington limit) tend to have H β blueshifted profiles due to radiation pressure-driven winds, while low accretion rate AGNs have symmetric lines due to less interference from such forces. Thus the model is consistent with observational trends (Negrete et al. 2018; Marinello et al. 2020). Strong outflow effects are more clearly observed in the high ionization lines like CIV λ 1549, which are emitted close to the continuum source and strongly affected by the radiation forces (e.g. Coatman et al. 2017; Martínez-Aldama et al. 2018; Temple et al. 2021). However, those lines forms in the High Ionization Line (HIL) region where line-driving (instead of dust-driving) dominates, and our model does not apply.

The figure 4 displays the line profiles, for the canonic model of AGNs, with the black hole mass set at $10^8 M_\odot$ accreting at Eddington rate (left panel) and for the model corresponding to the mean quasar properties (higher black hole mass and lower Eddington ratio, right panel) from Shen et al. (2011), as a function of the observer's viewing angle, ranging from 10° up to 60° (measured from the symmetry axis). The most noticeable effect here is broadening of the line profiles as the viewing angle increases as more of the BLR's rotational motion is projected along the line of sight. The behavior of the line peak, however, is quite complex and reflects the direction of the outflow. The blueshift mostly dominates but the red wing is very sensitive to the viewing angle.

3.2.2. Parameters of line shape

Line shapes are most frequently characterized either by FWHM, or by the standard deviation, σ . These two simple parametrization are not equivalent, and they reflect in particular the predominantly Gaussian or Lorentzian shapes, as discussed in detail by Collin et al. (2006). Since the model provides us with the full line shape, we can study how these shapes are reflected in the usual standard parametrization.

The figure 5 shows the relationship between the standard deviation, σ , and the FWHM of emission lines and other global parameters for a representative fixed viewing angle. As can be seen, there is a positive correlation between these two quantities, suggesting that systems with broader emission lines (higher FWHM) also tend to have larger σ . Models with higher Eddington ratios generally have smaller σ and FWHM, while those with lower accretion rates have larger σ values. It also shows a clear increasing trend of σ with black hole mass, while the FWHM is more complex, although both parameters show a negative correlation with the Eddington ratio. If we concentrate on the case of a fixed Eddington ratio of 0.3, which is usually considered as a transition from low to high Eddington sources (e.g. Laor & Netzer 1989; Campitiello et al. 2019), we see that the model for this Eddington ratio gives the σ of $\sim 1000 \text{ km s}^{-1}$ for the black hole mass of $10^7 M_\bullet$, while for larger mass, $10^9 M_\bullet$, is twice that high. It well aligns with the transition between Seyfert 1 galaxies and Narrow Line Seyfert 1 galaxies at FWHM of $\sim 2000 \text{ km s}^{-1}$ (those are less massive sources) (Peterson 2011; Paliya et al. 2024), and transition between type A quasars and type B quasars (those are more massive sources) at FWHM of $\sim 4000 \text{ km s}^{-1}$ (Marziani et al. 2003). The correlation between the FWHM and the accretion rate constrains the results into a defined region with some outliers. The negative relationship between the Eddington ratio and the FWHM (or black hole mass) is more visible in this panel, constraining the low black hole mass objects into the high accretion regime. This result resembles the behavior of the optical Eigenvector 1 (EV1) sequence (Boroson & Green 1992;

Sulentic et al. 2000; Marziani et al. 2003; Shen & Ho 2014), which correlates the FWHM and optical FeII strength, defined by the equivalent width ratio of FeII emission at 4434-4684 Å over H β , $R_{\text{FeII}} = \text{EW}(\text{FeII } \lambda 4570) / \text{EW}(\text{H}\beta)$. The linear relationship between R_{FeII} and the Eddington ratio (Zamfir et al. 2010), allow us a comparison with the observational findings. However, in the observational case, the region with low accretion rates and low FWHM is populated, which is not observed in our results constrain the predictions into a defined region.

The ratio of the FWHM to σ in line shape studies is known as the shape factor or form factor. This ratio provides information about the shape of the spectral line, and is commonly used to determine whether a line profile is closer to a Gaussian, Lorentzian, or else. For a Gaussian distribution, the shape factor is approximately 2.35, and for a Lorentzian distribution, the ratio approaches to zero. For a rectangular function, the ratio is equal 3.46, and a triangular function has a ratio of 2.45. Similarly, for an edge-on rotating ring, it gives a ratio of 2.83 (Collin et al. 2006). The behavior of the shape factor as a function of Eddington ratio, black hole mass, and viewing angle is shown in figure 6.

The results show that as the accretion rate increases, the shape factor decreases, especially for higher mass black holes. At low accretion rates, the shape factor is relatively high, indicating that the line profiles tend to be more Gaussian. This suggests that in these conditions, the broad-line region (BLR) gas has a more uniform velocity distribution, leading to a symmetric, Gaussian-like profile. As the accretion rate increases, the shape factor drops down, especially more pronounced for the higher mass black holes, suggesting that the line profiles become increasingly Lorentzian. This implies that at high accretion rates, the BLR has a more extended velocity distribution, leading to profiles with broader wings, characteristic of Lorentzian shapes. This trend could be attributed to the effect of radiation pressure (and also stronger turbulent motions) at higher accretion rates, leading to a more chaotic pattern of motion in the BLR, which broadens the wings of the emission lines. The change in the gas distribution as a function of the FWHM and Eddington ratio has been widely explored in the EV1 context, where sources with $\text{FWHM} < 4000 \text{ km s}^{-1}$ tend to show Lorentzian profiles and high accretion rates, while sources with $\text{FWHM} > 4000 \text{ km s}^{-1}$ show Gaussian distributions and low accretion rates (Sulentic et al. 2000). The observational findings agree with our predictions, including the effects of the high radiation pressure (Negrete et al. 2018). The change of the shape factor does not happens at a fixed Eddington ratio but explicitly depends also on the black hole mass. There is, however, a disagreement between the model and the trends known well from the data for small black hole mass $10^7 M_\bullet$. The model clearly underestimates the outflow velocity in low mass systems, and even for high Eddington ratio the line shape is strongly double-peaked, as too small vertical velocity leads to BLR remaining close to the disk surface, with the motion strongly dominated by the Keplerian motion. However, the position of the BLR is consistent with the data trends, and lines are narrow.

Similarly, as the black hole mass increases, for a fixed accretion rate the shape factor tends to decrease. The trend is stronger (starts at smaller black hole masses) for higher accretion rates. For lower black hole masses, the shape factor tends to remain closer to the Gaussian value, indicating a more symmetric velocity distribution of gas around smaller black holes. For more massive black holes, the shape factor drops, especially at high accretion rates. This means that the line profiles become more Lorentzian, likely due to broader wings in the emission lines,

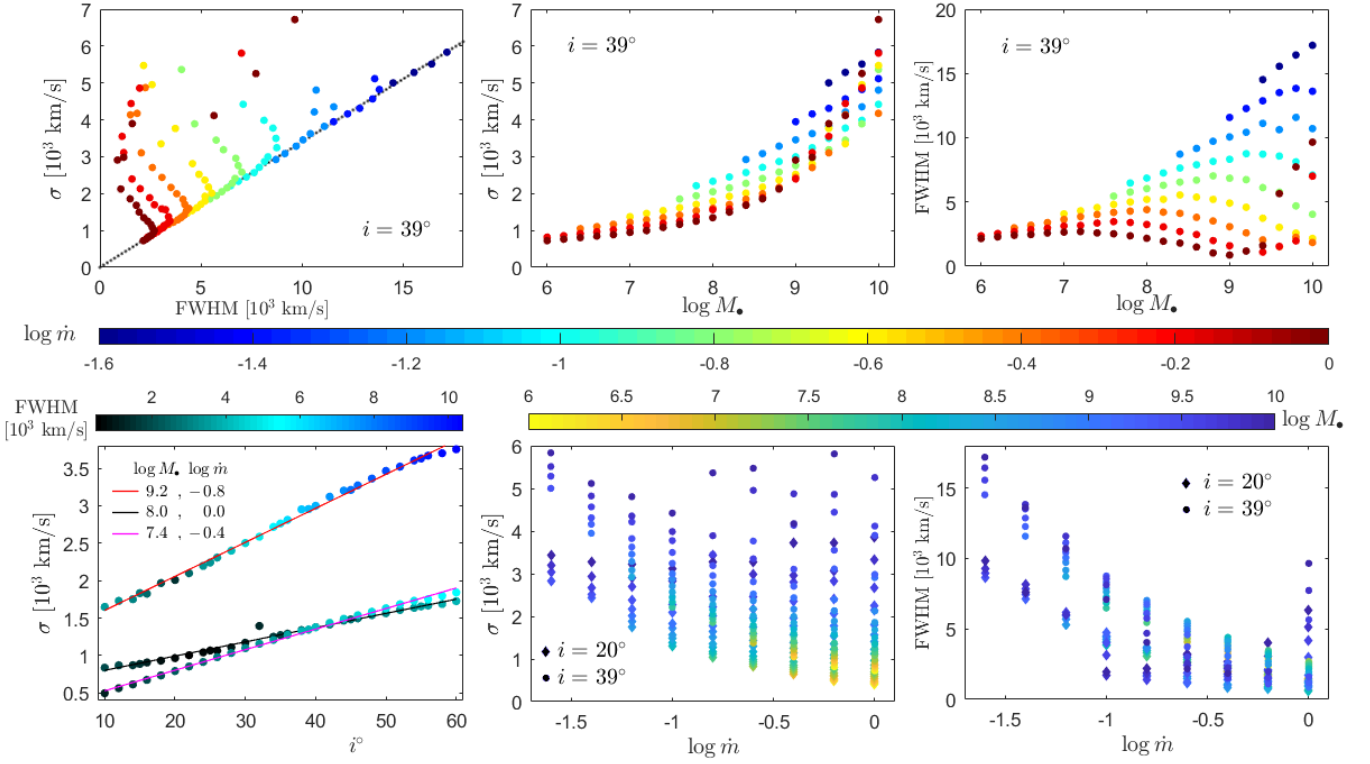


Fig. 5. Relations between σ and FWHM, and the predicted dependence on the black hole mass, accretion rate, and viewing angle. The black dotted line stands for an arbitrary linear fit, $\sigma = 0.34$ FWHM, to the trend of the underneath of data points in top-left panel. The solid lines in the bottom-left panel are also linear fits to the data points.

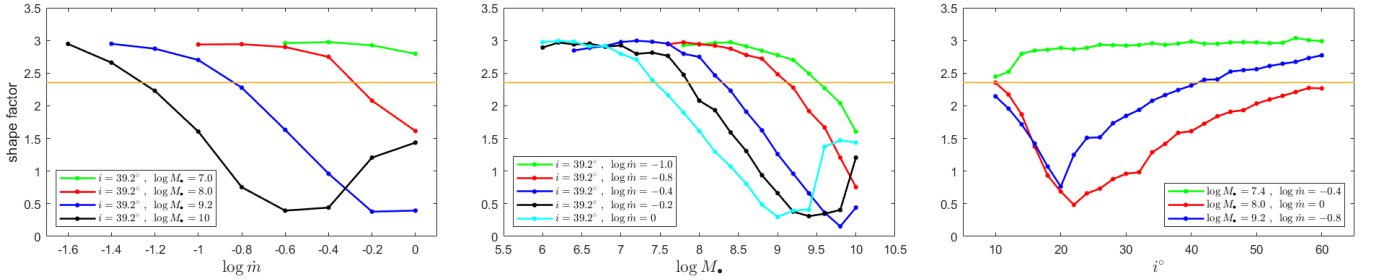


Fig. 6. The behavior of shape factor, the ratio of FWHM to σ , with respect to accretion rate, and black hole mass of the source, and also versus the observer's viewing angle. Orange line marks the value expected for a Gaussian line shape and separates Gaussian-like profiles (upper part of the plots) from Lorentzian-like profiles (lower part of the plots).

caused by more extreme velocity distributions at higher black hole masses. It may seem not intuitive. But for large black hole masses, like $10^9 M_\odot$, typical for quasars, the model predicts that there should be two quasar populations, with either Gaussian or Lorentzian shapes, and the transition is predicted to happen at $\dot{m} \sim 0.16$. This corresponds well to the division of quasars into type A (below the orange line in Fig 6) and type B (above the orange line in Fig. 6, middle panel). For lower masses the model predicts only Gaussian shape due to too small outflow velocities discussed above.

The shape factor is also affected by the viewing angle, it shows a minimum at intermediate viewing angles (around 20° to 25°), especially for higher black hole masses. At low viewing angles, the shape factor remains relatively close to 2.355, implying that the emission lines appear more Gaussian from a face-on perspective. This suggests that the BLR appears more symmetric when observed from low angles. As the viewing angle increases beyond 30° , the shape factor rises again, particu-

larly for more massive black holes. This suggests that for more edge-on views, the profiles again become more Gaussian, possibly due to projection effects that compress the velocity field into a more symmetric profile. The minimum around intermediate angles may arise from a combination of projection effects, and the more complex geometry of the BLR with formation of an outflow structure at higher black hole masses, higher Eddington ratios, where the line-of-sight intersects regions of the BLR with higher velocity dispersion, leading to Lorentzian-like profiles.

4. Time-delay and R-L relation

4.1. Method of determining the time delay and construction of the R-L relation

From the grid of simulations, we have the 3-D distribution of the clouds representing the geometry of the BLR based on the FRADO model. This distribution allows us to calculate how the radiation emitted in the most central region propagates to the

clouds and subsequently reaches the observer. The effect depends not only on the 3-D distribution and emissivity of each cloud but also on the viewing angle of the observer. The time of reprocessing of the radiation within each cloud is neglected since this is a rather fast process in comparison to propagation across the entire BLR zone.

Short pulse from the most central region thus reaches an observer in the form of the extended signal coming from all the clouds which can be stored in the form of the histogram, representing the BLR transfer function. The example of such transfer function is shown in the left panel of figure 7. It assumes that all the clouds are visible to the observer, and no shielding is included. However, we can also experiment with assumptions that some parts of the clouds are not directly visible. With this aim, we divided the clouds into those representing the far side and the near side. In cylindrical coordinates, We define the *near side* as comprising all clouds within the azimuthal range $0 \leq \phi < \pi$, which corresponds to the near-facing vertical half of the BLR cake closer to the observer. Conversely, the *far side* consists of clouds in the range $\pi \leq \phi < 2\pi$. Likewise, in Cartesian coordinates, taking the observer line-of-sight (arbitrarily due to azimuthal symmetry) in x-z plane, clouds with negative-positive x component are considered as far-near side of the BLR with respect to observer. We thus consider three histograms for each solution.

These histograms were analyzed to extract two key statistical quantities: the average time delay τ_{avg} , and the peak time delay τ_{peak} . The results are shown in figure 8. The full histograms are always highly asymmetric, in general double-peaked, with sharper first peak from the near side, and more shallow and extended peak from the far side of the BLR. Decomposition shows this clearly.

4.2. Results

The theoretical R-L relation depends significantly on the options outlined in section 4.1. Strong asymmetry leads to a considerable difference between the peak of the transfer function and the average time delay. Also selective shadowing of the close or far side would change the time delay estimate. We thus study some combinations and compare the results to the observed trends. In observations, the time-delays are usually measured with one of the standard methods, without reconstruction of the transfer function, therefore we do not know a priori which method is more appropriate to compared with the observed R-L.

4.2.1. average time-delays option

We analyze first R-L based on the the average time-delays. The results for a fixed representative viewing angle of 39° but all considered values of the black hole mass and Eddington rate are shown in figure 8, left upper corner. The black hole mass is not directly shown in the plot as for a fixed Eddington ratio it can be inferred from the luminosity so that lower luminosity corresponds to lower black hole mass. The results diverge from the observational trends, though the slope and overall distance is promising. Specifically, the average time-delay values displayed a behavior opposite to that expected from the R-L relation regarding the accretion rates. Delays are shorter for low Eddington rate (and they are similar quantitatively to the relation of Bentz et al. (2013)), but they are predicted to be longer for higher accretion rates while observations show the opposite (e.g. Du et al. 2015a). This suggests that while the average time delay provides

a general sense of the BLR's overall structure, it may be less sensitive to the actual emission-line response observed in real AGNs, especially when averaged over complex BLR dynamics.

We also explored potential biases that might have arisen due to noise in the observed BLR transfer functions. To address this, we tested removing particles in the simulation with a BLR response ratio below 10% of the peak, which was designed to minimize any spurious contributions from regions of the BLR that are weakly coupled to the continuum variations. Despite this adjustment, the issue with the average time-delays did not resolve.

4.2.2. peak time-delays option

When focusing on the peak values of the time-delay histograms, we observed strong consistency with the observed $H\beta$ R-L relation. The slope of the radius-luminosity relation obtained from our peak time-delays aligns well with the empirical data, indicating that the FRADO model can accurately capture the distribution of material and the dynamic response of the BLR gas. Importantly, the spread in the predicted time-delays which is thought to be dependent to the accretion rate of the sources, also follows the trends observed in real AGNs, although the observed spread is much larger than what we see in our simulations. This suggests that peak time-delays can be the robust indicator of dynamics and geometry of BLR. In figure 8 we plot delays separately from near and far side of the distribution, separately for each viewing angle. The difference between the far and near side time delay is rising strongly with the viewing angle, which is expected. The near-side lags tend to fall below the standard R-L relation (Bentz et al. 2013) due to shorter light travel times, while far-side lags lie closer to or above it.

4.2.3. R-L relation

The observed R-L relation should combine all viewing angles but looking at the separate panels of figure 8 we see qualitatively that we will not produce the observed spread if we use all the models. Much shorter time delay for high Eddington ratio can be accommodated in the model when, selectively, we choose only near side of the BLR for high Eddington sources. It is not the same scenario as proposed by Wang et al. (2014a) where the disk is shielding the BLR region close to the equatorial plane and the outflow is practically conical, thus shortening the time delay both for close and far side. Here we would have to postulate that some medium covers the far side of the BLR. Such a mechanism is not built into FRADO.

5. Virial factor

The virial factor (commonly denoted as f , also called correction factor) plays a critical role in estimating the mass of a super-massive black hole in AGNs using reverberation mapping techniques. Assuming a flattened disk-like BLR with predominantly Keplerian motion, the black hole mass, M_\bullet , is typically estimated using the virial equation

$$M_\bullet = f \frac{R_{\text{BLR}}}{G} \Delta V^2 \quad (1)$$

where R_{BLR} is the radius of the broad line region (measured via reverberation mapping), ΔV is representative of velocity of particles in the BLR, G is the gravitational constant, and f is the virial factor which accounts for uncertainties related to the geometry, kinematics, and inclination of the BLR in AGNs. Modeling of the BLR in 2.5D FRADO lets us directly find the virial factor.

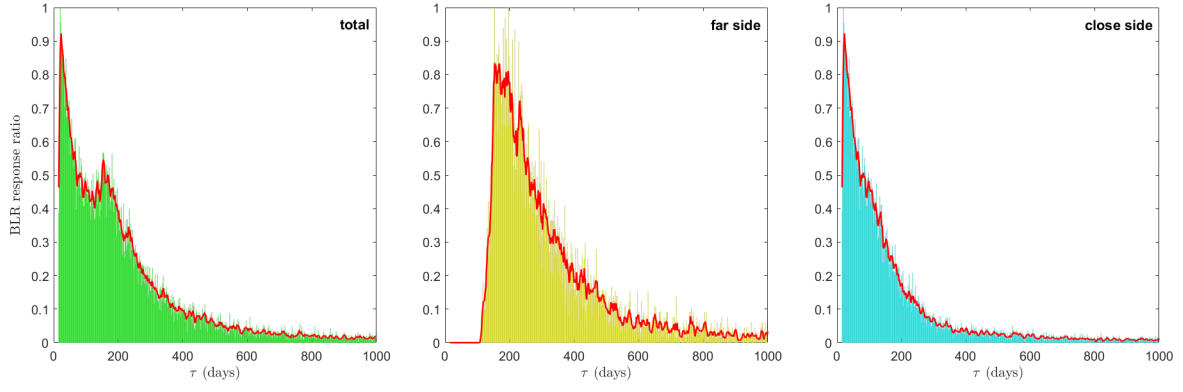


Fig. 7. Time-delay histogram for a model corresponding to the mean quasar viewed at 39° .

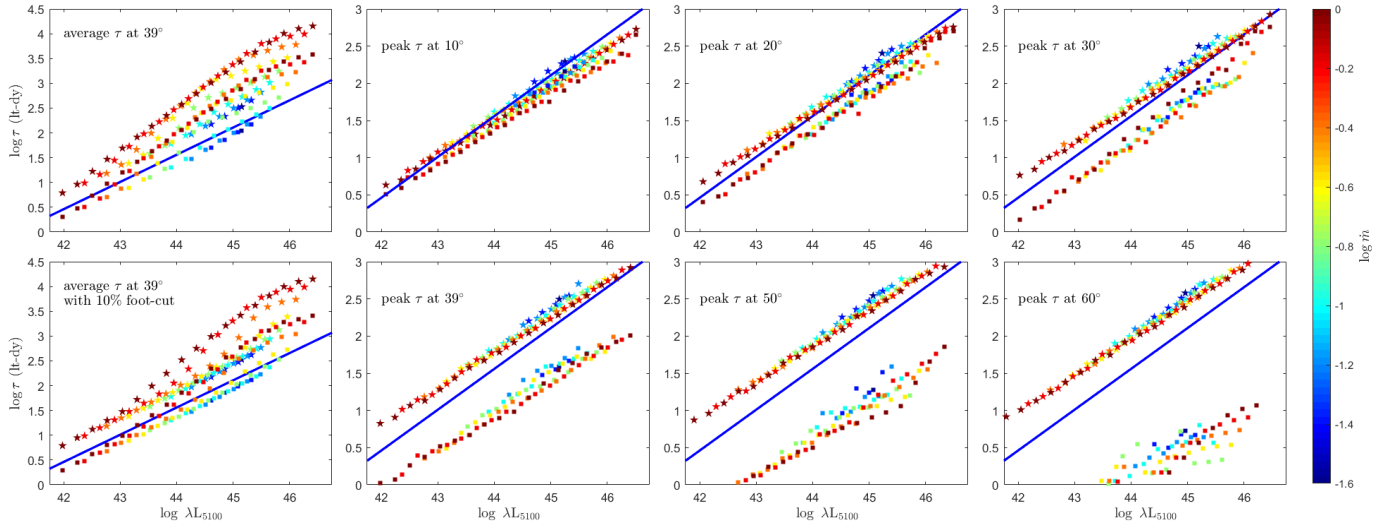


Fig. 8. R–L relation for various viewing angles and BLR configurations, for the two options of measuring the time-lags: average values (leftest two panels) and peak values (other panels). The blue line in each panel represents the empirical R–L relation calibrated for low accretors from (Bentz et al. 2013), the fully corrected fit with slope of 0.546 and interception value of 1.559. Color-coded data points correspond to different Eddington ratios as indicated by the colorbar. Pentagrams represent the far side of BLR relative to the observer, while squares correspond to the near side.

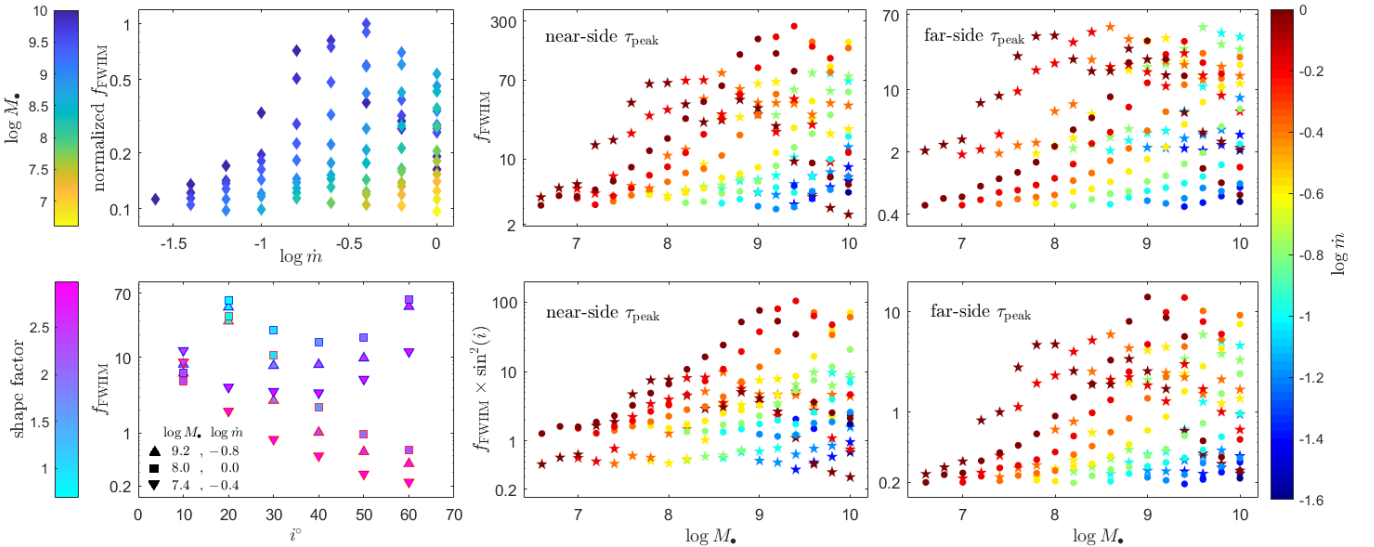


Fig. 9. Dependence of f_{FWHM} , predicted by 2.5D FRADO on Eddington ratio, black hole mass, viewing angle, and shape factor. Pentagrams and circles in four right panels represent the viewing angle of 20° , and 39° , respectively. In the top-left panel, the f_{FWHM} is shown vs. Eddington ratio for the far-side viewed at 60° . In the bottom-left panel, f_{FWHM} based on the far-side and near-side time-delays distinguished by edge colors of red and blue, respectively, is shown vs. viewing angle.

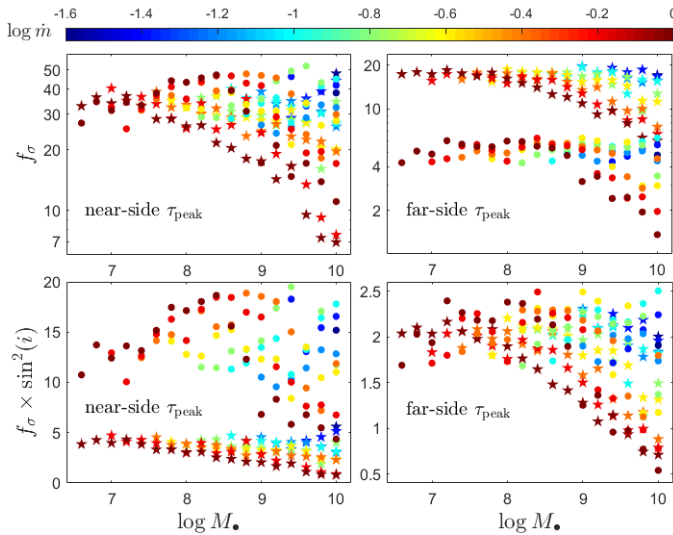


Fig. 10. Dependence of f_σ , predicted by 2.5D FRADO on Eddington ratio and black hole mass. Pentagrams and circles in four right panels represent the viewing angle of 20° , and 39° , respectively..

5.1. virial factor based on FWHM

If we consider the observed FWHM of the broad emission line to be representative of velocity range of particles in the BLR, one can find f via

$$f_{\text{FWHM}} = \frac{G M_\bullet}{c \tau} \frac{1}{\text{FWHM}_{\text{obs}}^2} \quad (2)$$

where FWHM_{obs} is the observed FWHM which may be related to that of intrinsic through $\text{FWHM}_{\text{obs}} \approx \text{FWHM}_{\text{int}} \cdot \sin(i)$ following (Collin et al. 2006), and i is the inclination angle, the angle between the observer's line of sight and the symmetry axis.

The results of dependence of f_{FWHM} , predicted by 2.5D FRADO on the black hole mass, Eddington ratio, viewing angle, and shape factor are presented in the figure 9. As obvious, the results imply a large departure of BLR from a virialized status. For low black hole masses low Eddington ratios, the f_{FWHM} starts at lower values and increases as these two parameters increase. There is a peak at black hole masses around $\log M_\bullet \sim 9.5$ for Eddington ratios around $\log \dot{m} \sim -0.4$. For higher black hole masses, f_{FWHM} decreases again, particularly for higher accretion rates. The behavior of f_{FWHM} appears to depend strongly on both black hole mass and Eddington ratio. The results also show that f_{FWHM} decreases with increasing viewing angle for all of the three representative models, showing an anti-correlation, especially for the results based on the far-side time-delays. The shape factor also show that at higher inclination angles the line profiles tend to be more Gaussian-like while at lower angles Lorentzian-like profiles are favored.

5.2. virial factor based on σ_{line}

On the other hand, one can rather use the velocity dispersion of particles in BLR, σ , to compute the virial factor as

$$f_\sigma = \frac{G M_\bullet}{c \tau} \frac{1}{\sigma_{\text{line}}^2} \quad (3)$$

Figure 10 shows the dependence of f_σ on black hole mass. As can be seen, f_σ . The range of f_σ in bottom-right panel of the figure, though with a noticeable scatter for high black hole

masses, spanning approximately from 0.5 to 2.5, is very well consistent with the general observational constraints of Onken et al. (2004); Collin et al. (2006) in which an squared sin factor is also included. The results in the top-left panel, if divided by 10, are also largely consistent with observational constraints, without introducing any inclination term. The other panels show that a strong segregation based on the viewing angle.

6. Discussion

The trends with the global parameters: black hole mass and Eddington ratio predicted by the FRADO model reproduce in an interesting way the trends observed in the data. Particularly the results for higher black hole masses (above $\sim 10^8 M_\odot$) are very promising. In case of very small black hole masses, $\sim 10^6 M_\odot$ the model seems to underestimate the intensity of the outflow. Below we address the successes and the shortcomings of the FRADO model in detail.

6.1. line profiles

6.1.1. black hole mass and line widths

Higher mass black holes produce broader emission lines due to the higher orbital velocities of gas in the BLR. This is consistent with the virial theorem, which links the velocity dispersion of the BLR gas to the black hole mass (e.g., Peterson et al. 2004).

6.1.2. accretion rate and line profile shape

While the accretion rate influences the overall intensity of the line emission, its effect on the profile shape in FRADO is less dramatic. Higher accretion rates tend to result in more asymmetric profiles, possibly due to winds or other outflow phenomena (e.g., Netzer 2013; Elvis 2000). As the accretion rate increases, radiation pressure can dominate and reduce the width of the line profile, often introducing asymmetry. At lower accretion rates, the disk is colder, the dust sublimation radius moves towards the black hole where the Keplerian rotation is faster, resulting in broader profiles due to higher orbital velocities in the BLR. This aligns with observational studies where AGNs with high accretion rates (near or above the Eddington limit) tend to have narrower profiles, while low accretion rate AGNs have broader lines due to less interference from such forces. FRADO also predicts the outflow, and its importance rises with the accretion rate, but this outflow is apparently underestimated for small black hole masses. This is seen in double-peak line profiles, predicted by FRADO for small black hole masses and high accretion rates, instead of observed single-peak Lorentzian shape for most Narrow Line Seyfert 1 galaxies. The line width is correct, which means that the launching radius is properly evaluated but the outflow or turbulence are not strong enough to remove the double-peak structure. We do not have a clear explanation of that. It may be that line driving plays a role when clouds are already launched but we need this extra force only for low mass objects. However, estimates of the role of the line driving force are beyond of the current paper. This would also require estimates of the filtering of the continuum through the inner High Ionization line region producing lines like HeII $\lambda 1640$ and CIV $\lambda 1549$.

6.1.3. viewing angle and profile broadening

The inclination of the BLR disk plays a crucial role in shaping the observed line profiles. Face-on views reveal the double-

peaked structure expected from a rotating disk, while edge-on views produce broader and more asymmetric profiles. This is consistent with models of disk-like BLR geometries (e.g., Gaskell 2009).

6.2. shape factor

As presented in the results, with the increase of accretion rate, the shape factor tends to decrease, especially for massive black holes, indicating a shift from more Gaussian profiles to Lorentzian-like profiles. This may be attributed to the increasing turbulence and velocity dispersion in the BLR gas at higher accretion rates (e.g., Sulentic et al. 2000). For higher black hole masses, the shape factor decreases, particularly at higher accretion rates. This suggests that the emission lines become broader and more Lorentzian-like for massive black holes, likely due to the stronger gravitational potential and more extreme velocity distributions in the BLR (e.g., Collin et al. 2006). The shape factor exhibits a minimum at intermediate viewing angles ($i \sim 25^\circ$), with Gaussian profiles being most prominent at low and high inclinations. This behavior can be linked to projection effects and the more complex geometry of the BLR with formation of an outflow structure at higher black hole masses, higher Eddington ratios, where the line of sight intersects regions of the BLR with higher velocity dispersion, leading to Lorentzian-like profiles. The shape factor is less sensitive to profile details than the presence or absence of a double-peak structure so the predicted trends are consistent with the discussion in Collin et al. (2006).

6.3. time-lags and R-L relation

The slope predicted by FRADO for low Eddington ratio sources is slightly flatter than canonical slope 0.5 expected from analytical FRADO (Czerny & Hryniewicz 2011) and the result by Bentz et al. (2013). However, this is not surprising, taking into account the newer results for the high Eddington ratio sources. The direct results from GRAVITY (GRAVITY Collaboration et al. 2024) which resolved BLR structure give a shallower slope than Bentz et al. (2013) and was consistent with higher accretion rates leading to shorter time-delays but the errors were large due to a small size of objects (four objects). Our model in its current version still underestimates the spread for high Eddington rate sources.

There may be several mechanisms at work which could lead to shortening of the time delay. At higher accretion rates, the inner disk region may become denser and more opaque. This can preferentially obscure the far side of the BLR, particularly due to self-absorption or scattering (Netzer & Marziani 2010; Wang et al. 2014b), or strong disk winds that can rise above the BLR and block the far side (e.g., Murray et al. 1995; Elvis 2000). Also black hole spin affects the monochromatic flux and the ionization parameter in a different way which could also play a role (e.g. Czerny et al. 2019).

The near-side of BLR appears literally closer, more projected to the observer and thus more luminous (in flux per unit area), particularly at intermediate to high inclinations (e.g., Goad & Korista 2014, 2015). Therefore the systematic scatter observed in the R-L relation for high-accretion-rate sources, can be attributed to the geometric and radiative weighting of the line response across the BLR. Specifically, our modeling suggests that this deviation correlates with a progressive dominance of near-side emission in the reverberation signal. But this geometrical effect can be applied to low accretors as well thereby we do see

some of them also deviating from the standard R-L relation of Bentz et al. (2013), however at high viewing angles for which the closer side of the BLR is obscured for the observer by dusty torus, the far side of the BLR still can be visible for low-accretors due to lack of inner opaque disk winds and strong outflows while in the case of high accretors the far side is not visible at any angle. That's why we can also find some observed low accretors located little above the standard R-L relation.

Comparing our results in figure 8 with the observational data (Martínez-Aldama et al. 2019) indicates that the maximum viewing angle at which the $H\beta$ is observed is 39 degree, and more than this angle either the $H\beta$ flux becomes very dim or the transition to type 1.5 AGNs happens. The results also imply that the standard R-L relation calibrated for low-accretors (Bentz et al. 2013) mainly include those sources viewed at very low viewing angles. In the next paper, we will go through comprehensive detailed on implications of this model for the R-L relation and quasar cosmology.

These results imply that accurate black hole mass estimations using the virial method based on FWHM need to account for many parameters including variations in the accretion rate, as it significantly influences the virial factor, especially in the intermediate and high-mass regimes.

On the other hand, line dispersion, σ , is often considered a more reliable measure of the BLR kinematics than FWHM, as can be concluded from the figure 10. This is because it captures the full range of velocities within the BLR, including random motions and contributions from all components of the line profile. Studies such as Peterson et al. (2004) have emphasized that σ yields more accurate black hole mass estimates and reduces scatter in the calibration of the virial factor. FWHM tends to measure the velocity of the bulk of the gas, but it can simply miss the contributions from high-velocity wings, which may result in underestimation of the black hole mass. Additionally, FWHM is more sensitive to projection effects. As also implied from our results in 10, line dispersion may lead to smaller uncertainties in black hole mass estimates. For example, Collin et al. (2006) argued that using σ rather than FWHM reduces scatter in the $M_\bullet - \sigma_\star$ relation too, the correlation between black hole mass and the velocity dispersion of the host galaxy's bulge.

There are important issues which are still not addressed in the current version of FRADO model. As we mentioned before, the vertical velocity for small black hole masses seem to be underestimated and we suspect it might be related to the line driving force. Our model launches clouds by the dust radiation pressure but perhaps line driving turns in as well, and we have no estimate of its role. Combining the two radiation pressure forces, however, is a challenge. The codes describing exclusively line driven winds exist (Risaliti & Elvis 2010; Quera-Bofarull et al. 2023) but they have different architecture and combining them will not be a simple task. Incorporating the role of line driving may also affect our conclusion about the metallicity. We use here the assumption of the metallicity five times higher than solar since otherwise the launching force seems too weak.

Finally, we do not specify what happens in the disk regions where the wind is not launched, and for low mass black holes this happens (in our computations) for low Eddington rates. In this case the disk surface can be directly irradiated by the central region which also could lead to formation of emission lines. On one hand, AGN disks are relatively flat and geometrically thin so direct irradiation may not be efficient (see e.g. Loska et al. 2004) but irradiation can be done by scattering in the highly ionized medium, for example warm absorber, as argued in the same work.

6.4. FRADO and microlensing

Since the 2.5D FRADO BLR model is able to reproduce a large variety of observed broad emission line profiles observed in AGN, it is also interesting to see if microlensing of the FRADO BLR can reproduce the line profile distortions observed in a number of gravitationally lensed AGN. A negative answer would imply a significant revision of the model.

Microlensing by stars in the lens galaxy of a lensed AGN is a phenomenon that can selectively magnify quasar subregions, in particular within the BLR, producing observable distortions in the emission line profiles that can be used to infer the size, geometry, and kinematics of the BLR. Based on generic BLR models, [Hutsemékers & Sluse \(2021\)](#), [Hutsemékers et al. \(2023, 2024a,b\)](#), and [Savić et al. \(2024\)](#) have shown that Keplerian disk and equatorial wind models best describe the geometry and kinematics of the BLR, while polar wind models can be ruled out. Using the physically based modeling of the BLR in 2.5D FRADO with well-defined initial source parameters (thus avoiding arbitrary parameterization of the BLR structure), we should be able to simultaneously fit both the line profiles and their distortions to further investigate the BLR properties and hopefully directly infer source parameters such as the black hole mass and/or the accretion rate.

As a first step, we used the method described in [Hutsemékers et al. \(2023, 2024a,b\)](#), and references therein), replacing the generic models with a 2.5D FRADO model of the BLR. We adopted a typical model with a black hole mass of 10^8 solar masses, an accretion rate of 0.1 in Eddington units and an inclination of 34° . The isovelocity maps generated by the 2.5D FRADO model were then convolved with microlensing magnification maps. For each position on the magnification map, a magnification profile $\mu(v)$ was computed, this profile representing the wavelength-dependent distortion of the emission line profile induced by the microlensing effect ($\mu(v) = 1$ indicates no distortion at all). The generated profiles were then selected to match a representative set of observed magnification profiles among those shown in ([Hutsemékers et al. 2023, 2024a,b](#); [Savić et al. 2024](#)). The observed profiles were scaled to a common velocity grid. Such profiles are shown in Fig. 11, demonstrating that microlensing of the 2.5D FRADO BLR model can reproduce the different line profile distortions observed in several lensed AGN; the blue and red wings can be either both magnified, both demagnified, or one magnified and the other demagnified. By comparing a large number of simulated line and magnification profiles with the observed ones, it would be possible to better constrain the BLR parameters than with generic models.

7. Conclusion

Following our previous work on the dynamical character and shape of LIL BLR based on the non-hydrodynamic single-cloud 2.5D FRADO model ([Naddaf et al. 2021](#)), we here tested the model by calculation of line profiles for the model-concluded distribution of clouds along their trajectories within LIL BLR, for a relatively large grid of initial conditions. The model well predicts the position of the inner radius of the BLR where clouds start to be launched. Predicted line shape factor is roughly consistent with observational trends, we also obtained interesting results for the virial factor. Line shapes are well modeled for larger black hole masses. R-L relation is well reproduced (both the position and the slope) for small Eddington ratios, in case of high Eddington ratio we could possibly recover the observed

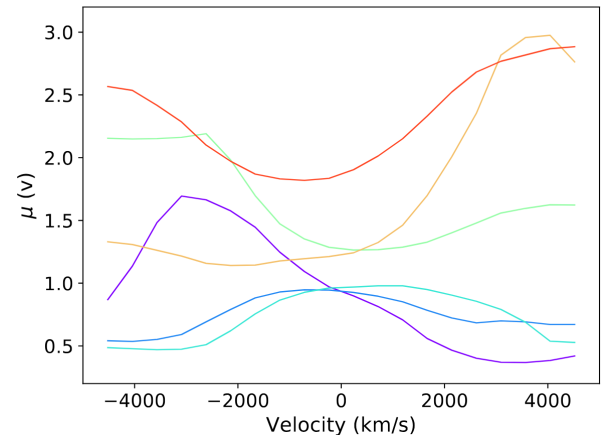


Fig. 11. Magnification profiles generated by microlensing a 2.5D FRADO model of the BLR. These profiles are selected to match observed profiles of different shapes.

trend when postulating some selective shielding of the far side of the cloud distribution.

Acknowledgements. This project is supported by the University of Liege under Special Funds for Research, IPD-STEMA Program. BC acknowledges the OPUS-LAP/GA "CR-LA bilateral project (2021/43/1/ST9/01352/OPUS 22 and GF23-04053L). MHN would like to thank Ashwani Pandey for the permission to use his part of CLOUDY results on dependence of H β on photon flux. MLMA acknowledges financial support from Millenium Nucleus NCN2023_002 (TITANs) an ANID Millennium Science Initiative (AIM23-0001).

References

- Antonucci, R. 1993, *ARA&A*, 31, 473
- Antonucci, R. R. J. & Miller, J. S. 1985, *ApJ*, 297, 621
- Baldwin, J. A. 1997, in *Astronomical Society of the Pacific Conference Series*, Vol. 113, IAU Colloq. 159: Emission Lines in Active Galaxies: New Methods and Techniques, ed. B. M. Peterson, F.-Z. Cheng, & A. S. Wilson, 80
- Barvainis, R. 1987, *ApJ*, 320, 537
- Baskin, A. & Laor, A. 2018, *MNRAS*, 474, 1970
- Bentz, M. C., Denney, K. D., Grier, C. J., et al. 2013, *ApJ*, 767, 149
- Bianchi, S., Antonucci, R., Capetti, A., et al. 2019, *MNRAS*, 488, L1
- Blandford, R. D. & McKee, C. F. 1982, *ApJ*, 255, 419
- Boroson, T. A. & Green, R. F. 1992, *ApJS*, 80, 109
- Campitiello, S., Celotti, A., Ghisellini, G., & Sbarrato, T. 2019, *A&A*, 625, A23
- Cao, S., Mandal, A. K., Zajaček, M., Czerny, B., & Ratra, B. 2024, *arXiv e-prints*, arXiv:2412.19665
- Cao, S., Zajaček, M., Panda, S., et al. 2022, *MNRAS*, 516, 1721
- Chatzikos, M., Bianchi, S., Camilloni, F., et al. 2023, *Rev. Mexicana Astron. Astrofis.*, 59, 327
- Coatman, L., Hewett, P. C., Banerji, M., et al. 2017, *MNRAS*, 465, 2120
- Collin, S., Kawaguchi, T., Peterson, B. M., & Vestergaard, M. 2006, *A&A*, 456, 75
- Cracco, V., Ciroi, S., Berton, M., et al. 2016, *MNRAS*, 462, 1256
- Czerny, B. & Hryniewicz, K. 2011, *A&A*, 525, L8
- Czerny, B., Hryniewicz, K., Maity, I., et al. 2013, *A&A*, 556, A97
- Czerny, B., Modzelewska, J., Petrogalli, F., et al. 2015, *Advances in Space Research*, 55, 1806
- Czerny, B., Olejak, A., Rałowski, M., et al. 2019, *ApJ*, 880, 46
- Czerny, B., Różańska, A., & Kuraszkiewicz, J. 2004, *A&A*, 428, 39
- Davies, R. I., Thomas, J., Genzel, R., et al. 2006, *ApJ*, 646, 754
- Du, P., Hu, C., Lu, K.-X., et al. 2015a, *ApJ*, 806, 22
- Du, P., Hu, C., Lu, K.-X., et al. 2015b, *ApJ*, 806, 22
- Du, P. & Wang, J.-M. 2019, *ApJ*, 886, 42
- Du, P., Zhang, Z.-X., Wang, K., et al. 2018, *ApJ*, 856, 6
- Eckart, A., Hüttemann, A., Kiefer, C., et al. 2017, *Foundations of Physics*, 47, 553
- Elitzur, M. & Ho, L. C. 2009, *ApJ*, 701, L91
- Elvis, M. 2000, *ApJ*, 545, 63
- Eracleous, M. & Halpern, J. P. 1994, *ApJS*, 90, 1
- Eracleous, M., Lewis, K. T., & Flohic, H. M. L. G. 2009, *New A Rev.*, 53, 133
- Ferland, G. J., Baldwin, J. A., Korista, K. T., et al. 1996, *ApJ*, 461, 683
- Gaskell, C. M. 2009, *New A Rev.*, 53, 140

- Genzel, R., Eisenhauer, F., & Gillessen, S. 2010, *Reviews of Modern Physics*, 82, 3121
- Gilbert, K. M. & Peterson, B. M. 2003, *ApJ*, 587, 123
- Goad, M. R. & Korista, K. T. 2014, *MNRAS*, 444, 43
- Goad, M. R. & Korista, K. T. 2015, *MNRAS*, 453, 3662
- Gravity Collaboration, Amorim, A., Bauböck, M., et al. 2021, *A&A*, 648, A117
- Gravity Collaboration, Amorim, A., Bauböck, M., et al. 2020, *A&A*, 643, A154
- GRAVITY Collaboration, Amorim, A., Bourdarot, G., et al. 2024, *A&A*, 684, A167
- Gravity Collaboration, Sturm, E., Dexter, J., et al. 2018, *Nature*, 563, 657
- Hicks, E. K. S. & Malkan, M. A. 2008, *ApJS*, 174, 31
- Hutsemékers, D. & Sluse, D. 2021, *A&A*, 654, A155
- Hutsemékers, D., Sluse, D., & Savić, Đ. 2024a, *A&A*, 687, A153
- Hutsemékers, D., Sluse, D., & Savić, Đ. 2024b, *A&A*, 691, A292
- Hutsemékers, D., Sluse, D., Savić, Đ., & Richards, G. T. 2023, *A&A*, 672, A45
- Kaspi, S., Smith, P. S., Netzer, H., et al. 2000, *ApJ*, 533, 631
- Khadka, N., Yu, Z., Zajaček, M., et al. 2021, *MNRAS*, 508, 4722
- Korista, K. T. & Goad, M. R. 2004, *ApJ*, 606, 749
- Kriss, G. A., De Rosa, G., Ely, J., et al. 2019, *ApJ*, 881, 153
- Krolik, J. H. 1999, *Active galactic nuclei : from the central black hole to the galactic environment*
- Laor, A., Jannuzi, B. T., Green, R. F., & Boroson, T. A. 1997, *ApJ*, 489, 656
- Laor, A. & Netzer, H. 1989, *MNRAS*, 238, 897
- Lawrence, A. & Elvis, M. 2010, *ApJ*, 714, 561
- Li, Y.-R., Wang, J.-M., Ho, L. C., Du, P., & Bai, J.-M. 2013, *ApJ*, 779, 110
- Liu, B. F. & Qiao, E. 2022, *iScience*, 25, 103544
- Liu, B. F., Yuan, W., Meyer, F., Meyer-Hofmeister, E., & Xie, G. Z. 1999, *ApJ*, 527, L17
- Loska, Z., Czerny, B., & Szczerba, R. 2004, *MNRAS*, 355, 1080
- Marinello, M., Rodríguez-Ardila, A., Marziani, P., Sigut, A., & Pradhan, A. 2020, *MNRAS*, 494, 4187
- Martínez-Aldama, M. L., Czerny, B., Kawka, D., et al. 2019, *ApJ*, 883, 170
- Martínez-Aldama, M. L., del Olmo, A., Marziani, P., et al. 2018, *A&A*, 618, A179
- Marziani, P., Zamanov, R. K., Sulentic, J. W., & Calvani, M. 2003, *MNRAS*, 345, 1133
- Moloney, J. & Shull, J. M. 2014, *ApJ*, 793, 100
- Moran, E. C., Halpern, J. P., & Helfand, D. J. 1996, *ApJS*, 106, 341
- Murray, N., Chiang, J., Grossman, S. A., & Voit, G. M. 1995, *ApJ*, 451, 498
- Naddaf, M. H. & Czerny, B. 2022, *A&A*, 663, A77
- Naddaf, M.-H. & Czerny, B. 2024, *Universe*, 10, 29
- Naddaf, M.-H., Czerny, B., & Szczerba, R. 2021, *ApJ*, 920, 30
- Naddaf, M. H., Martínez-Aldama, M. L., Marziani, P., et al. 2023, *A&A*, 675, A43
- Negrete, C. A., Dultzin, D., Marziani, P., et al. 2018, *A&A*, 620, A118
- Netzer, H. 2013, *The Physics and Evolution of Active Galactic Nuclei* (Cambridge, UK: Cambridge University Press)
- Netzer, H. & Marziani, P. 2010, *ApJ*, 724, 318
- Nicastro, F., Martocchia, A., & Matt, G. 2003, *ApJ*, 589, L13
- Onken, C. A., Ferrarese, L., Merritt, D., et al. 2004, *ApJ*, 615, 645
- Onken, C. A., Valluri, M., Peterson, B. M., et al. 2007, *ApJ*, 670, 105
- Paliya, V. S., Stalin, C. S., Domínguez, A., & Saikia, D. J. 2024, *MNRAS*, 527, 7055
- Pancoast, A., Brewer, B. J., & Treu, T. 2011, *ApJ*, 730, 139
- Pancoast, A., Brewer, B. J., Treu, T., et al. 2012, *ApJ*, 754, 49
- Pandey, A., Czerny, B., Panda, S., et al. 2023, *A&A*, 680, A102
- Peterson, B. M. 1993, *PASP*, 105, 247
- Peterson, B. M. 2011, *arXiv e-prints*, arXiv:1109.4181
- Peterson, B. M. 2014, *Space Sci. Rev.*, 183, 253
- Peterson, B. M., Ferrarese, L., Gilbert, K. M., et al. 2004, *ApJ*, 613, 682
- Peterson, B. M., Wanders, I., Horne, K., et al. 1998, *PASA*, 110, 660
- Quera-Bofarull, A., Done, C., Lacey, C. G., Nomura, M., & Ohsuga, K. 2023, *MNRAS*, 518, 2693
- Risaliti, G. & Elvis, M. 2010, *A&A*, 516, A89
- Rózańska, A. & Czerny, B. 2000, *MNRAS*, 316, 473
- Sabra, B. M., Shields, J. C., Ho, L. C., Barth, A. J., & Filippenko, A. V. 2003, *ApJ*, 584, 164
- Savić, Đ. V., Hutsemékers, D., & Sluse, D. 2024, *A&A*, 687, A114
- Schmidt, M. 1963, *Nature*, 197, 1040
- Seyfert, C. K. 1943, *ApJ*, 97, 28
- Shen, Y. & Ho, L. C. 2014, *Nature*, 513, 210
- Shen, Y., Richards, G. T., Strauss, M. A., et al. 2011, *ApJs*, 194, 45
- Sulentic, J. W., Marziani, P., & Dultzin-Hacyan, D. 2000, *ARA&A*, 38, 521
- Temple, M. J., Ferland, G. J., Rankine, A. L., Chatzikos, M., & Hewett, P. C. 2021, *MNRAS*, 505, 3247
- Véron-Cetty, M. P., Véron, P., & Gonçalves, A. C. 2001, *A&A*, 372, 730
- Wang, J.-M., Qiu, J., Du, P., & Ho, L. C. 2014a, *ApJ*, 797, 65
- Wang, J.-M., Qiu, J., Du, P., & Ho, L. C. 2014b, *ApJ*, 797, 65
- Watson, D., Denney, K. D., Vestergaard, M., & Davis, T. M. 2011, *ApJ*, 740, L49
- Zamfir, S., Sulentic, J. W., Marziani, P., & Dultzin, D. 2010, *MNRAS*, 403, 1759